# PCCP

www.rsc.org/pccp

**PERSPECTIVE**

# Perspectives on Raman spectroscopy of graphene-based systems: from the perfect two-dimensional surface to charcoal

**Ado Jorio and Luiz Gustavo Cançado**

Raman spectroscopy has been already established as a powerful tool for characterizing the different types of carbon nanostructures, ranging from the highly ordered two-dimensional graphene and one-dimensional nanotubes, down to disordered materials, like nanographite and charcoal. Here we focus on the recent advances of Raman spectroscopy within carbon nanoscience. We discuss *in situ* nano-manipulation and Raman imaging for addressing controlled perturbations; multi-technique work for the development of nanometrology; crossing the diffraction limit with near-field optics for high resolution imaging. Finally, the applications of Raman spectroscopy in cross-referenced fields, like biotechnology and soil science, are discussed.

## 1.  Introduction – historical achievements

The Raman spectroscopy has played a very important role in the development of the science related to carbon nanostructures for different reasons: (i) due to the unusually large surface-to-volume ratio, nanostructures are especially sensitive to the environment, including the probes used for their study. Light is a massless and chargeless probe, weakly perturbing the nanostructures; (ii) Raman spectroscopy is the inelastic scattering of light, mostly due to vibrational modes (phonons, see Fig. 1), experimentally simpler to perform when compared to most of the techniques in nanoscience and nanotechnology, non-destructive, being used for *in situ* experiments, requiring almost no sample preparation; (iii) vibrational modes in carbon nanostructures strongly modulate the Raman polarizability tensor, guaranteeing a strong response; (iv) due to the high stiffness of the σ bonds, the Raman spectra exhibit peaks with relatively high frequencies, so that any tiny (less than 1%) frequency change is easily detectable. Therefore, the phonons are an excellent probe for sensing and characterizing gentle structural or electronic modifications; (v) due to the special π electronic structure, the scattering processes are usually resonant, making the intensity even higher and making it possible to study both phonons and electrons. Multiple resonances enhance special scattering processes, which allow the Raman spectroscopy to go beyond its usual role in materials and molecular science. With all these

*Departamento de Física, Universidade Federal de Minas Gerais, Belo Horizonte, MG, Brazil. E-mail: adojorio@fisica.ufmg.br, cancado@fisica.ufmg.br; Fax: +55 31 34095600; Tel: +55 31 34096610*

**Ado Jorio**

*Ado Jorio is a Full Professor in the Department of Physics, at the Federal University of Minas Gerais, having received his PhD in Physics at the same institution, in 1999. He spent two years at the Massachusetts Institute of Technology (2000–2001), USA, as a post-doctoral fellow and since then works on the optical properties of nanomaterials, focusing on the Raman spectroscopy of carbon nanostructures, in which he has authored over 150 scientific articles and three books. Recently his interests cover interdisciplinary work (soil, biology and medical sciences) and scientific instrumentation.*

**Luiz Gustavo Cançado**

*Luiz Gustavo Cançado is an Adjunct Professor at the Physics Department of the Federal University of Minas Gerais (UFMG), Brazil. He received his PhD degree in 2006, at the same University, studying Raman spectroscopy of nanographites. He spent three years (2007–2009) at the Institute of Optics (University of Rochester) as a post-doctoral fellow in the Nano-optics group. He is currently interested in tip-enhanced Raman spectroscopy applied to graphene and carbon nanotubes. He also works on the metrology of defects in nanocarbons.*
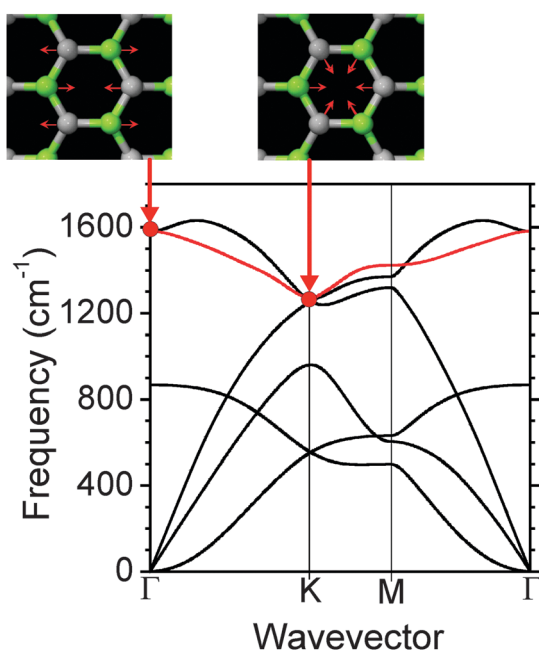
**Fig. 1** Phonon dispersion for graphene. The eigenvectors for the first-order Raman allowed mode, the G band, and for the K point phonon, related to the disorder induced D band and its second order G′ (or 2D) are shown on the top.[2] The D and G′ bands come from the in-plane transverse optical (iTO) phonon branch (painted in red). Accurate theoretical description of the optical phonons at the $\Gamma$ and K point was only possible after introducing the Kohn anomaly in graphene science.[27]

aspects in mind, it is easy to understand why carbon was present at the discovery of the Raman scattering effect, in the late twenties,[1] and it still keeps its influence on the development of experimental Raman spectroscopy, being largely applied nowadays to study and characterize new forms of carbon nanostructures and their applications.[2]

The use of Raman spectroscopy to characterize nanocarbons has a milestone in the early seventies, in the field of nano-graphite and amorphous carbons,[3] crossing important applications in the field of ion implantation and graphite intercalation compounds,[4] fullerenes[5] and carbon nanotubes.[6] With the advances on the synthesis and the worldwide spread of nanoscience tools, an impressive development in this field took place in the first decade of the 21st century.[7] From 2000 to 2009, one can easily list a great number of achievements based on the use of Raman spectroscopy to study and characterize nanocarbons. In our view, some of the major breakthroughs of this decade were: the qualitative description of the amorphization trajectory from graphite to tetrahedral amorphous carbon by Ferrari and Robertson;[8] the introduction of the double resonance mechanism to explain the disorder induced D band in defective graphite by Thomsen and Reich[9] and the further extension of this model to other phonons by Saito et al.;[10] the study of one-dimensional selection rules by Rao et al.;[11,12] the launch of single nanotube spectroscopy by Jorio et al.[13] and the realization of single graphene nanoribbon spectroscopy by Cançado et al.;[14] the demonstration of how the second-order Raman spectra provide information about changes in the electronic structure of carbon nanotubes by Souza Filho et al.[15] and the application of this knowledge to determine the number of layers in graphene by

Ferrari et al.;[16] the observation of tip enhanced Raman spectroscopy (TERS) from carbon nanotubes by Hartschuh et al.;[17] the use of Raman spectroscopy to define graphite edge structure by Cançado et al.[18] and extension of this finding to graphene by Casiraghi et al.;[19] the determination of the optical transitions for single-walled carbon nanotubes (SWNTs) by Fantini et al.,[20] Telg et al.,[21] Araujo et al.[22] and Doorn et al.,[23] and for double-wall carbon nanotubes (DWNTs) by Pfeiffer et al.;[24] the study of doping in carbon nanotubes by Souza Filho et al.[25] and Corio et al. with electrochemistry;[26] the introduction of the Kohn anomaly physics in graphene and graphite by Piscanec et al.[27] (see Fig. 1), and its applications to understand and characterize doping in both graphene[28] and carbon nanotubes;[29,30] the introduction of many-body physics for accurate description of the Raman matrix elements in SWNTs by Jiang et al.;[31] the TERS study of single doping/defect in a single wall carbon nanotube structure by Maciel et al.;[32] the introduction of environmental effects in both vibrational[33] and electronic properties[34] of SWNTs by Araujo et al.

Each topic listed in the previous paragraph was followed by a large number of publications from several different groups around the world.[2,7] It is, therefore, a very good time to evaluate what is the role of Raman spectroscopy from carbon nanostructures nowadays, and which are the paths for the developments in this field in this coming decade.

## 2. Pushing the limits

To push the limits of Raman spectroscopy and its applications to carbon nanoscience, some routes are in place: (i) *in situ* nanomanipulation and Raman imaging of nanocarbons, introducing well-controlled perturbations to study intrinsic and extrinsic properties; (ii) multi-technique work for the development of quantitative and highly accurate results, *i.e.* for the development of nanometrology; (iii) crossing the diffraction limit with near-field optics, to address single events within a single nano-system, localized below the light diffraction limit. In this section we describe each item.

### 2.1 *In situ* nanomanipulation and Raman imaging

The ability to perform nanomanipulation and Raman spectroscopy is important for a well-controlled study of intrinsic and extrinsic properties of nano-structures. Here we provide two examples: (1) the study of graphene superlattices, which happens when two graphenes are placed on top of each other, forming the so-called Moiré pattern. (2) The study of transversal pressure in carbon nanotubes which breaks the circumferential symmetry.

**2.1.1 Folding graphene to build graphene superlattices.** Superlattice structures are generated in bilayer graphene by a mismatch angle $\theta$ between the top and bottom layers.[35] Low energy van Hove singularities (VHSs) appear in the DOS of such superlattices[36] and the distance between these VHSs can be tuned by controlling the mismatch angle $\theta$ between layers. The possibility to control these singularities open new paths for electronic engineering, while the presence of VHSs near the Fermi energy can generate interesting electronic instabilities.[37–39]

Fig. 2 shows the formation of graphene superlattice by folding graphene into itself with an atomic force microscopy tip.[40] Fig. 2a shows the G band intensity imaging, which is
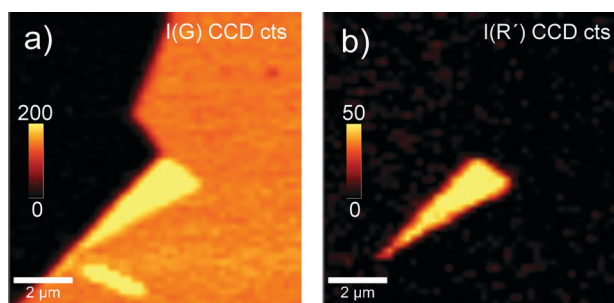
**Fig. 2** Raman image of graphene folded into itself. (a) G band intensity; (b) R′ band intensity, showing the presence of the graphene superlattice formed by a mismatch angle $\theta = 6°$ between the two layers. The angle was defined using eqn (1) and confirmed by atomic resolution AFM.[40]

twice in the area where the graphene is folded, showing that two graphene layers are scattering at this area (triangle in Fig. 2a). The superlattice formation was shown to activate new Raman modes from the interior of the graphene phonon Brillouin zone.[40–43] They have been called R (from "rotation") when related to a double resonance inter-valley process, appearing below the G band frequency, and R′ when related to a double resonance intra-valley process, appearing above the G band frequency.[40] Fig. 2b shows an image in the spectral range where the new R′ band is observed. It appears only in the folded region, showing it is an effect of the superstructure.

The mismatch angle $\theta$ between the two layers was measured with atomic resolution atomic force microscopy (AFM), and the frequency of the R′ peak was shown to depend on $\theta$, so that Raman spectroscopy can indubitably define the super-lattice structure. Equations can be built to relate $\theta$ with the R or R′ Raman frequency:

$$\theta = 1026 - 1.25\omega_R + 0.00038\omega_R^2;$$

$$\theta = 3378 - 4.35\omega_{R'} + 0.0014\omega_{R'}^2. \qquad (1)$$

The R′ band used to build Fig. 2b was observed at $\omega_{R'} = 1625$ cm$^{-1}$. Using eqn (1) we obtain $\theta = 6.12°$, which has been confirmed by atomic resolution AFM measurements.[40]

Furthermore, the G band intensity was shown to exhibit a large intensity enhancement for specific values of $\theta$ and excitation laser energy $E_L$.[44–46] This effect happens due to resonance achieved with the new VHSs in the electronic density of states, showing that Raman spectroscopy can probe the energy difference between the two VHSs in the valence and conduction bands which have been induced by the superlattice structure. The G′ band lineshape also changes with changing $\theta$ and $E_L$, reflecting the changes in the electronic structure, as previously introduced for carbon nanotubes,[15] and in sequence for $N$-layers graphene.[16]

**2.1.2 Pressing carbon nanotubes to study elasticity.** Raman spectroscopy has been largely used to study environment or intentionally induced structural changes in graphene-based materials.[2,7] More specifically, Raman spectroscopy has been used to study effects caused by strain, majorly focusing on the G-band behaviour on SWNT bundles.[47–53] The effect of hydrostatic pressure on SWNT bundles has then been defined

as an upshift in the G-band frequencies for low pressure values, followed by broadening and further disappearance of the G-band signal when increasing pressure. Circumferential symmetry breaking (ovalization) and tube collapse are expected at higher pressure values, and these effects have been invoked to explain, respectively, the broadening and disappearance of the G-band signal. Experiments on isolated SWNTs have also been performed, but dealing with uniaxial strain along the tube axis,[48,49] without addressing the effect of circumferential deformation.

Araujo et al.[54] used a home built system that combines AFM with confocal Raman spectroscopy to follow, in situ, the evolution with applied transversal pressure of the G-band feature in isolated SWNTs deposited on a substrate (see Fig. 3). The left panel in Fig. 3 shows the result of molecular dynamics calculation. The tube ovalization happens when pressing the SWNT. The right panel in Fig. 3 shows the appearance of a new feature in the G-band profile when applying transversal pressure on one isolated SWNT, by compressing the tube with an AFM tip against the substrate where it is sitting. By changing the pressure slowly, the new peak was shown to be a splitting of the lower frequency TO G-phonon. Therefore, a previously elusive and fundamental symmetry-breaking effect was observed for the totally symmetric TO G-band mode, which exhibits two distinct Raman-active features with increasing applied pressure, one localized at the flattened regions, the other localized at the curved regions of the ovalized SWNT. Different SWNTs showed different behaviours, such as a G+/G− (mixed LO/TO) frequency splitting followed by peak broadening. The measured tubes exhibited different chiral angles, and this explains the different G-band behaviours, since the TO vs. LO nature of the vibrational modes in SWNTs depend on chirality. This work thus evidenced the richness of transversal deformation at the isolated SWNT level,[54] which are averaged on SWNT bundle measurements.

## 2.2 Multi-technique work for the development of nanometrology

In Section 2.1, the Raman signature for graphene superlattices was discussed. To obtain eqn (1), relating a Raman frequency with the structural angle $\theta$, the Raman response had to be calibrated with microscopy information at the atomic level (AFM in the case of ref. 40 and TEM in ref. 46). This multi-technique approach
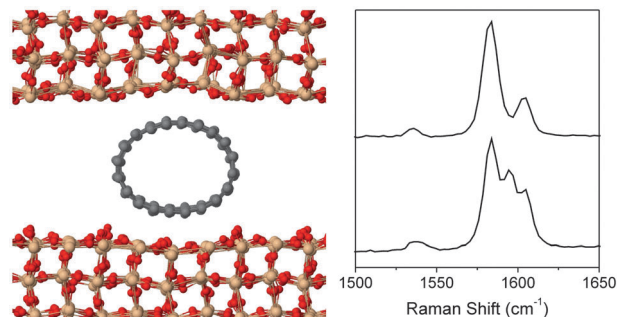


**Fig. 3** Left: cross-sectional view of a (10,0) nanotube compressed between two identical SiO$_2$ blocks, as used in the molecular dynamics simulations. Right: G-band profiles before applying pressure (top) and during the strongest pressure level (bottom).[54]

is crucial for the development of Raman spectroscopy based nanometrology. Here we will discuss three examples: (1) the use of Raman combined with scanning tunnelling microscopy (STM) to calibrate the Raman based signature of defects in graphene; (2) Raman combined with scanning electron microscopy (SEM) and electric field microscopy (EFM) to characterize the effects of a focused ion beam (FIB) on graphene; (3) the use of transmission electron microscopy (TEM) to calibrate the SWNT diameter dependence of the radial breathing mode resonance Raman cross-section, so that Raman can be used as an accurate measure of SWNT diameter distribution in a sample.

### 2.2.1 Raman combined with STM for quantifying defects in graphene.

Raman spectroscopy is one of the most sensitive techniques that can be used to characterize disorder in the $sp^2$ network of carbon materials. It is widely used to identify disorder in diamond-like carbon, amorphous carbon, nano-structured carbon, carbon nanofibers, carbon nanotubes and carbon nanohorns.[3,4,8,55,56] The most important signature is the intensity ratio between the G band (1585 cm$^{-1}$) and the disorder-induced D band (1345 cm$^{-1}$ for $E_L$ = 2.41 eV), $I_D/I_G$. Although the proposal of the amorphization trajectory for graphite was in place since 2000,[8] it was only after the rise of graphene that the Raman spectroscopic signature of the amorphization trajectory was measured experimentally.[57] Lucchese et al.[57] performed consecutive ion-bombardment procedures to gradually induce disorder in graphene, followed by Raman spectroscopy $I_D/I_G$ characterization (see Fig. 4). The ion dose and the average distance between defects ($L_D$) were independently calibrated by scanning tunnelling microscopy (STM) experiments (see the inset to Fig. 4). This study was extended to the disorder evolution of all Raman modes,[58] $N$-layer graphene[59] and graphite.[60] Other groups also measured the effects of bombardment in graphene.[61,62]

This type of study was developed previously in graphite.[4] The novelty about graphene is that, in this one-atom thick material, the results are ind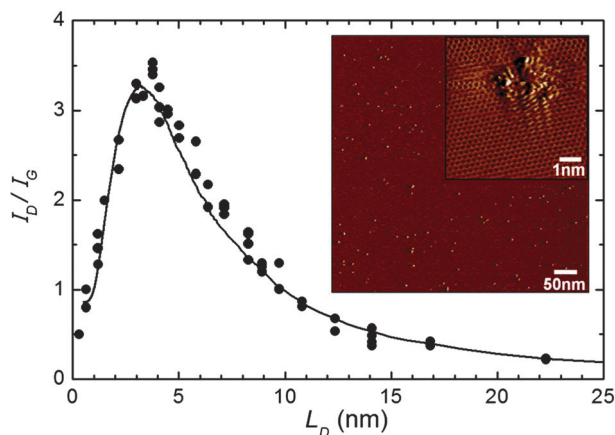ependent of the penetration depths for both the incident light and ions. These analyses lead to the formulation of a phenomenological model for the quantification of disorder in graphene,[57] which is in conceptual agreement with the amorphization trajectory proposed by Ferrari and Robertson for graphitic nano-crystallites.[8] The model describes the evolution of the Raman-based disorder signature $I_D/I_G$ when decreasing the average distance between defects ($L_D$ in Fig. 4), or crystalline size as reported in ref. 8. The graphene results showed that the Tuinstra–Koenig relation,[3] or the analogue but most accurate version introduced later,[63,64] should be limited to measure nanocrystallite size, but should not be applied for a quantitative analysis of point-like defects in graphene. The evolution of peak frequencies, intensities, line-widths and areas of the main Raman bands of graphene were analyzed as a function of bombardment dose and number of layers.[58] The Raman relaxation length for the disorder-induced Raman scattering process in graphene was established as 2 nm,[57] a value that is at least 10 times more accurate than the values previously published in the literature.[65,66]

This work was extended to study the effect of low energy (90 eV) Ar$^+$ ion bombardment in graphene samples as a function of the number of layers $N$.[59,60] The evolution of the intensity ratio $I_D/I_G$ with ion fluence was determined for mono-, bi-, tri- and $\sim$50-layer graphene samples, providing a spectroscopy-based method to study the penetration of these low energy Ar$^+$ ions in AB Bernal stacked graphite, and how they affect the graphene sheets.[59]

In sequence, the $I_D/I_G$ dependence on the excitation laser energy $E_L$, already established for nanographite,[63,64] was extended to point defects in graphene,[67] thus providing a formula for quantifying the amount of defects in graphene for any excitation laser energy. In terms of defect density $n_D$ (cm$^{-2}$) = $10^{14}/(\pi L_D^2)$ and the laser wavelength $\lambda_L$ (in nm) we have[67]

$$n_D \text{ (cm}^{-2}) = [(1.8 \pm 0.5) \times 10^{22}/\lambda_L^4] (I_D/I_G). \quad (2)$$

### 2.2.2 Raman combined with SEM and EFM to characterize the effects of a focused ion beam on graphene.

A different perspective from what has been presented in Section 2.2.1, where another technique is used to calibrate the Raman response, is the use of the Raman response to study and to calibrate instruments and procedures. Archanjo et al.[68] discussed the use of a Ga$^+$ focused ion beam (FIB) to modify graphene for device applications. Their motivation relies on proving suitable characteristics of Ga$^+$ FIB sources. They had already shown[69] that Raman spectroscopy is more sensitive than AFM and scanning electron microscopy (SEM) for characterizing defects in graphene, as it is able to measure the effects of ion bombardment in graphite structure for fluencies down to $10^{11}$ ions per cm$^2$.

In order to determine the ion dose for which the graphene sheet can have a totally insulating line, as well as the lateral damaged area, linear patterns with different ion doses were produced in a single layer graphene sample, as shown by SEM in Fig. 5a.[68] The dwell time was changed from 1 μs up to 1 ms [from left to right in Fig. 5a)], and the ion dose was varied from $6 \times 10^{12}$ to $6 \times 10^{15}$ ions per cm$^2$, accordingly. Table 1 shows the dwell time, ion dose and lateral profile for each line made in the graphene sample. The dwell time, and consequently the ion dose, was increased from left to right in Fig. 5. A higher dose



**Fig. 4** Intensity ratio between the G band and the D band ($I_D/I_G$) in graphene as a function of the average distance between defects ($L_D$), created by Ar$^+$ bombardment. The inset shows an STM image of the ion bombarded graphene, used to calibrate the ion bombardment procedure, giving accurate information about $L_D$.[57] A similar plot for the D′ band (another disorder-induced feature at $\sim$1620 cm$^{-1}$) is presented in ref. 58.
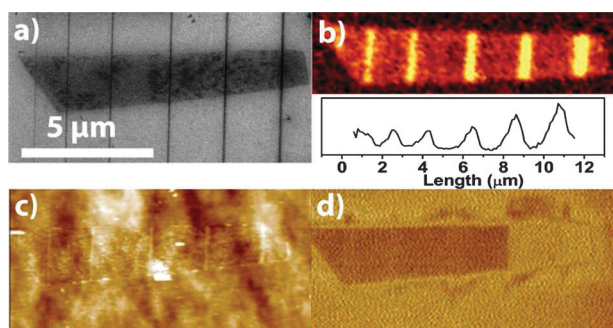
**Fig. 5** Graphene with 6 focused ion beam (FIB) patterned lines using different ion doses, increasing from left to right; (a) SEM image; (b) Top: Raman map of the integrated intensity of the D band. Bottom: intensity line profile of the Raman map; (c) AFM image of the sample; (d) electric force microscopy (EFM) image of the sample after charging, showing that there is no charge after the fifth line.[68]

led to a broader line, as can be seen from the two-dimensional map of Raman D peak intensity shown in Fig. 5b.

To address the problem of the minimum dose necessary to generate an insulating line, charge injection experiments using electric force microscopy (EFM) were performed. Fig. 5c and d show the AFM and EFM images, respectively. As shown in Fig. 5d, no charge was transferred through the fifth line. Hence, as shown in Table 1, they found that $3 \times 10^{15}$ ions per cm$^2$ is the minimum dose needed to create an insulating line in the graphene layer.

To address the problem of the lateral damage, they used Raman spectroscopy imaging to obtain the lateral damaged width of a bombarded line and compared it to the line width directly obtained from the SEM image (Table 1). By deconvoluting the D band response and the point spread function of the incident laser from the D band intensity profile, they were able to estimate the lateral damaged widths in the fifth and sixth lines as $90 \pm 20$ nm and $350 \pm 70$ nm, respectively, which are much higher than what the SEM could image. This is an important result for the development of graphene nanostructures using Ga$^+$ FIB, since it shows that one must consider this lateral damaged width in order to obtain the correct shape when making an insulating region, or completely removing graphene areas.

**2.2.3 Raman combined with TEM for quantifying SWNT diameters in a sample.** The multi-technique approach has also been used in the study of single-wall carbon nanotubes (SWNTs) Raman spectroscopy. The Raman spectra from the radial breathing modes (RBMs) have been largely used to give information about the diameter distribution in the samples.[2,7] However, it is known that the Raman cross-section itself depends strongly on the tube diameter, mostly due to the

diameter dependence of the excitonic effects.[31] Pesce *et al.*[70] used a high resolution transmission electron microscopy (HRTEM) protocol to measure the SWNT diameter distribution in a bundle sample, and compared the results with the RBM resonance Raman map. This procedure was used to calibrate the diameter dependence of the RBM Raman cross-section, thus establishing a method for accurate determination of the diameter distribution in a SWNT sample.

In this study,[70] single-wall carbon nanotubes (SWNTs) grown by the water-assisted chemical vapour deposition (CVD) method was used as a standard sample.[33,34] HRTEM measurements of 395 SWNTs determined the diameter distribution of the sample, allowing calibration of a resonance Raman scattering radial breathing mode (RBM) map obtained with 51 laser excitation energies from 1.26 eV to 1.73 eV (see Fig. 6). Thus, the diameter dependence of the resonance Raman scattering RBM cross-section was determined, which in turn allows the determination of the diameter distribution of any SWNT sample by measuring the RBM Raman signal. Since each RBM spectrum $[S(\omega, E_L)]$ is the sum of the individual RBM contributions of all SWNTs, it can be written as:[70]

$$S(\omega, E_L) = \Sigma_{n,m}\{Pop_{(n,m)}I_{(n,m)}\Gamma/2/[(\omega - \omega_{RBM})^2 + (\Gamma/2)^2]\} \quad (3)$$

where $Pop_{(n,m)}$ is the population of the (n,m) nanotube species, $\Gamma = 3$ cm$^{-1}$ is the experimental average value for the full width at half maximum intensity of the tube's RBM Lorentzian, $\omega_{RBM}$ is the frequency of its RBM, $\omega$ is the Raman shift, and $I_{(n,m)}$ is a function of the excitation laser energy $E_L$, which for the Stokes process is given by

$$I_{(n,m)} = |M/[(E_L - E_{ii} + i\gamma)(E_L - E_{ph} - E_{ii} + i\gamma)]|^2, \quad (4)$$

where $E_{ph} = \hbar\omega_{RBM}$ is the energy of the RBM phonon, $E_{ii}$ is the energy corresponding to the *i*-th excitonic transition, $\gamma$ is a damping factor, and $M$ represents the matrix elements for the Raman scattering by one RBM phonon of the (n,m) nanotube. The $M$ and the $\gamma$ values can be found in ref. 70, while the $\omega_{RBM}$ and $E_{ii}$ parameters have been synthesized in ref. 71, including environmental effects.

### 2.3 Crossing the diffraction limit with near-field optics to address localized events

The advantage of using near-field optics to image nanostructures is illustrated in Fig. 7, which brings the optical imaging of a carbon nanotube. While panel (a) shows the confocal blurred G band Raman image of a SWNT, panel (b) shows the near-field G band Raman image of the blue square in panel (a). In (a) the resolution is one order of magnitude higher than that in (b), allowing to realize that the tube has a loop

**Table 1** A summary of FIB dwell time, ion dose and lateral line width taken from different techniques for each bombarded line[68]

| Line | 1 | 2 | 3 | 4 | 5 | 6 |
|---|---|---|---|---|---|---|
| Dwell time (μs) | 1 | 10 | 50 | 100 | 500 | 1000 |
| Dose (ions per cm$^2$) | $6 \times 10^{12}$ | $6 \times 10^{13}$ | $3 \times 10^{14}$ | $6 \times 10^{14}$ | $3 \times 10^{15}$ | $6 \times 10^{15}$ |
| Profile width$^a$ (nm) | $23 \pm 2$ | $35 \pm 4$ | $40 \pm 4$ | $40 \pm 4$ | $49 \pm 5$ | $72 \pm 7$ |
| Profile width$^b$ (μm) | $0.65 \pm 0.06$ | $0.65 \pm 0.06$ | $0.68 \pm 0.07$ | $0.63 \pm 0.06$ | $0.74 \pm 0.07$ | $1.0 \pm 0.1$ |

$^a$ Profile width obtained directly from the SEM image. $^b$ Profile width obtained from the Raman profile plot in Fig. 5b.
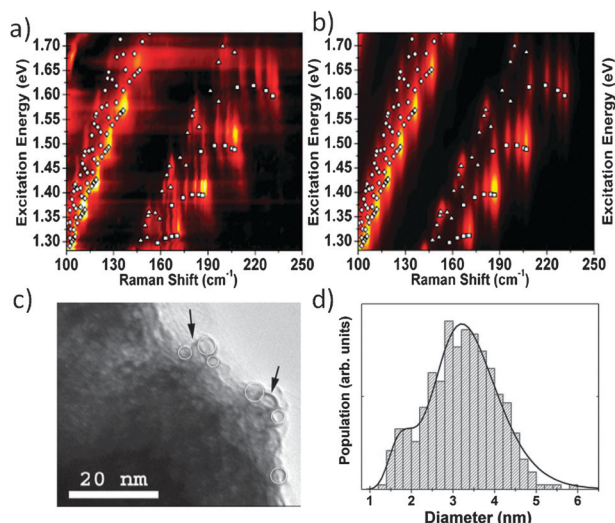
**Fig. 6** (a) Experimental resonance Raman scattering map of the radial breathing mode from SWNTs; (b) theoretical map using the parameters described in ref. 70. (c) High resolution TEM image from the sample, showing the cross section of some SWNTs, used to measure the tube diameters (white circles). (d) SWNT diameter distribution in the sample, obtained by high resolution TEM from 395 physically different SWNTs, using the TEM automated procedure for SWNT diameter measurement described in ref. 70.

morphology. This image is generated by scanning a nano-antenna (a gold AFM tip) on top of the surface, generating the so-called tip-enhanced Raman spectroscopy (TERS) effect, bringing here the spacial resolution of $\sim 10$ nm.

Since the application of near-field optics is still in an early stage in solid state physics, chemistry and materials science, this section starts with a short tutorial description of the effect, and in the later subsection we discuss the state-of-the art of near-field Raman spectroscopy applied to carbon nanoscience.

**2.3.1 The basics for near-field optics.** The spatial resolution for the optical analysis is limited by two phenomena: aberration and diffraction. Aberration is related to the optical quality of the system, and it occurs when light from one point of the sample under analysis does not converge into a single point in the detector after transmission through the optical system (similarly, if light reaching the detector does not diverge from a simple point in the sample). These effects lead to blurring of
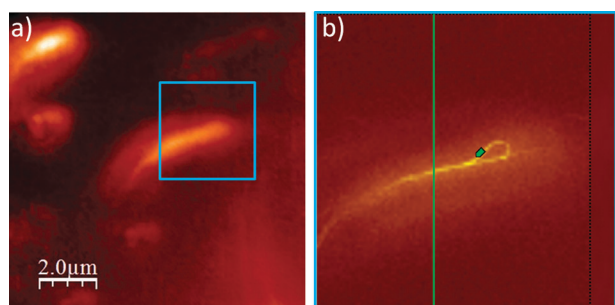


**Fig. 7** (a) Confocal G band image of a SWNT. (b) Tip enhanced Raman spectroscopy (TERS) G band image of the area marked with the blue square in (a). Unpublished data measured in the Nano-Spectroscopy Laboratory at UFMG.

the image in the detector, and the image blurring can be ameliorated by increasing the optical quality of the system.

Diffraction is a fundamental physics limitation coming from the wave nature of light. On this matter, the spatial resolution of an optical system can be defined as the minimum distance that two points can be close to each other before they become optically indistinguishable because of diffraction. A standard for defining the special resolution is the Abbé criterion, which states that this minimum distance is given when the central maximum of the diffraction pattern from a circular aperture of one imaged point falls below the first minimum of the other. This determines a resolution[72]

$$r = 0.61\lambda/\text{NA}, \qquad (5)$$

where $\lambda$ is the radiation wavelength and NA the objective numerical aperture. Since $r$ is proportional to $\lambda$, blue light can be focused to a smaller spot than red light. $r$ is also inversely proportional to NA, which in turn depends on the index of refraction of the medium, $n$. The maximum NA is typically 1.45 when using an immersion oil lens with a refractive index of $n = 1.52$. In an air objective, the maximum NA is typically smaller, leading to lower spatial resolution. Furthermore, to achieve the maximum resolution for a given NA, the laser beam has to be expanded to fully cover the active area of the lens. Due to these limitations, the resolution limit of a confocal light microscope using visible light is about 200 nm, *i.e.* it does not reach the nanoscale.

To overcome this limitation, one has to access the so-called near-field regime. The limitation described above is related to the Fourier properties of a lens. The angular spectrum representation of a scattered electric field $E_s$ in a plane $z = $ constant far from the light source (far-field regime) is given by[73,74]

$$E_s(x, y, z)$$
$$= \int\int_{-\infty}^{\infty} \hat{E}_s(k_x, k_y; 0) \exp\{i(k_x + k_y)\} \exp\{i(k_z - \omega t)\} dk_x dk_y$$
$$(6)$$

where $k_x$, $k_y$ and $k_z$ are the spatial frequencies related to the Cartesian coordinates $x$, $y$, and $z$, respectively, and $\hat{E}_s(k_x, k_y; 0)$ are the Fourier amplitudes of the electric field at $z = 0$.

The exponential term $\exp\{i(k_z - \omega t)\}$ in eqn (6) describes the propagating electric field $E_s$ along the $z$-axis. Without neglecting the $k_x$ and $k_y$ components, the $\boldsymbol{k}$-vector $(k_x, k_y, k_z)$ and the frequency $\omega = 2\pi c/\lambda$ are related by the free-space dispersion relation, so that[73,74]

$$k_z = \text{sqrt}\{(2\pi n/\lambda)^2 - (k_x^2 + k_y^2)\} \qquad (7)$$

According to eqn (6) and (7), there is a limit for $(k_x^2 + k_y^2)$ to generate a propagating field. For $(k_x^2 + k_y^2) \leq 2\pi n/\lambda$, the wave vector $k_z$ is a real number. In this case, the electric field $E_s$ propagates along the $z$-axis oscillating with $\exp\{ik_z\}$, giving rise to the far-field component of the optical field. On the other hand, if $(k_x^2 + k_y^2) > 2\pi n/\lambda$, the wave vector $k_z$ becomes an imaginary number, the electric field $E_s$ decays exponentially along the $z$ direction, and the contribution from this decaying part (evanescent waves – the near-field) is generally lost.

For visible light, the evanescent waves decay within a few nanometers. Therefore, conventional optical systems are not able to collect the whole spectrum of spatial frequencies associated with optical fields generated by a light source located at a distance sufficiently far from the detector (far-field regime). However, spatial resolutions down to $r = 10$ nm have already been achieved using near-field optical systems. These systems combine optics with scanning probe technology, so that the evanescent waves can contribute by approaching the light source/detector very close to the sample (within the nm range).

**2.3.2 Near-field Raman in graphene-like nanocarbons.** Near-field Raman scattering applied to graphene-like nanocarbons initiated in 2003 on carbon nanotubes,[17,75] making use of the tip-enhanced Raman spectroscopy (TERS) technique.[17,32,74] Due to their low dimensionality and huge optical response, carbon nanotubes have been widely used as prototype samples for the development of TERS. Some results achieved in carbon nanotubes were nanoscale vibrational analysis,[76] nanoscale optical imaging of excitons,[77] TERS polarization measurements,[78] imaging of nanotube chirality changes,[79] spectral determination of single charged defects,[32] local optical response of semiconducting nanotubes to DNA-wrapping,[80] among others. A comprehensible review can be found in ref. 74.

In the case of graphene, a few results are appearing in the literature,[81–84] including the imaging of defects and contaminants.[85] However, TERS in two-dimensional systems has special complexity that has to be treated theoretically.

Theory describing the near-field Raman enhancement has been initially developed for one-dimensional systems (applicable to carbon nanotubes),[86] and recently extended for two-dimensional (2D) systems (applicable to graphene).[87] The near-field Raman intensity was quantified as a function of the tip–sample distance. Considering the tip position determined by the tip–sample distance $\Delta$, and the tip radius $\rho_{tip}$, the near field signal obeys[87]

$$I_{NF} \propto (\Delta + \rho_{tip})^{\ell}. \qquad (8)$$

The interaction length is roughly defined by the tip radius $\rho_{tip}$ and hence the scattering process is in the coherent case if the phonon coherence length $L_{ph} \gg \rho_{tip}$, while in the incoherent case if $L_{ph} \ll \rho_{tip}$. Table 2 provides the parameter $\ell$ ruling the tip–sample distance dependence [eqn (8)] of the near-field Raman intensity in zero-dimensional, one-dimensional, and two-dimensional systems, considering both coherent and incoherent scattering regimes.

The study was extended to consider incident laser beam configuration, and tip orientation relative to the sample plane, which was shown to be important for graphene.[87] The theoretical calculations show that playing with the tip orientation might be important in the two-dimensional case. Fig. 8(a) shows the plot of the total incoherent scattered intensity of the G mode as a function of $\theta$ (see angle definitions in the right side of Fig. 8). The solid (blue) and dashed (red) lines were obtained considering radially and linearly polarized laser modes, respectively. For the radially polarized mode, the scattered intensity is clearly higher for low $\theta$ angles (tip vertically positioned), being maximum at $\theta \approx 15°$, and minimum (but not null) at $\theta \approx 95°$ (tip horizontally positioned). For the linearly polarized mode, the condition for the maximum

**Table 2** Summary of the tip–sample distance dependence of the near-field Raman intensity ($I_{NF}$) in zero-dimensional (0D), one-dimensional (1D), and two-dimensional (2D) systems. The numbers are the powers $\ell$ in eqn (8) for both coherent and incoherent scattering regimes[87]

|  | 0D | 1D | 2D |
| --- | --- | --- | --- |
| Coherent | −12 | −10 | −8 |
| Incoherent | −12 | −11 | −10 |

scattered intensity is achieved for $\theta \approx 45°$. However, it is clear from the figure that even in this case the near-field signal intensity is much higher (about ten times) if the radially polarized laser mode is applied. Fig. 8b shows the same analysis for the total coherent scattered intensity. For the radially polarized mode, the scattered intensity reaches the maximum value at $\theta \approx 60°$, while for the linearly polarized mode the maximum scattered intensity is achieved for $\theta \approx 80°$. The maximum value for the scattered intensity is considerably higher for the radially polarized laser mode. In both cases (radially and linearly polarized laser modes), the coherent scattered intensity is null for $\theta = 0$ due to interference effects.

## 3. Applications

In this article, we have already discussed several applications of Raman spectroscopy in carbon nanoscience, which falls basically on the use of the technique to provide a simple characterization tool for the structural and electronic aspects of the $sp^2$ nanocarbons. Raman scattering gives the spectroscopic signatures for each carbon nanostructure, quantifying defects, deformations, doping, *etc*. It is a prototype for the development of nanometrology. In this section we focus on applications in the fields of biotechnology and soil science, to show how Raman spectroscopy can help to develop cross-related fields.
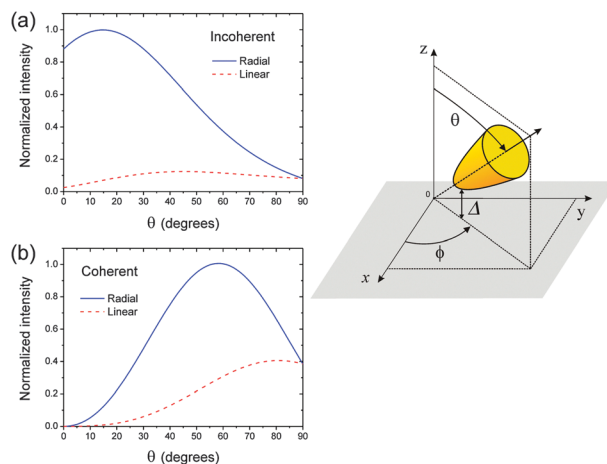


**Fig. 8** Calculated Raman intensity considering tip induced near-field enhancement as a function of the inclination angle $\theta$ between the tip dipole orientation and the surface normal (see schematic figure on the right). Both radial and linearly polarized lights are plotted. (a) Total *incoherent* scattered intensity of the G mode. The solid (blue) and dashed (red) lines were obtained considering radially and linearly polarized laser modes, respectively. (b) Total *coherent* scattered intensity of the G mode.[87] The inclination angle $\theta$ should not be confused with the mismatch angle between two rotationally stacked graphene layers, as defined in Section 2.1.1.

15252 | *Phys. Chem. Chem. Phys.*, 2012, **14**, 15246–15256

This journal is © the Owner Societies 2012

### 3.1 Carbon nanotubes in Biotechnology

Carbon-nanotube-based carriers are one of the non-viral vectors that have gained increasing interest as a safer and cost-effective delivery system for gene materials, including plasmid DNA (pDNA) and oligonucleotides (ODN), as well as proteins and peptides. Different studies have evaluated the ability of SWNTs and multi-wall carbon nanotubes (MWNTs) as transfection agents, *i.e.* to introduce nucleic acids into cells, delivering gene materials, including pDNA, ODN, proteins and peptides.[88–91]

For the development of RNA interference technology, positively charged –CONH–(CH$_2$)$_6$–NH$^{3+}$Cl-functionalized SWNTs were shown to be able to bind and efficiently carry short interfering RNA sequences (siRNA) into tumour cells,[90] to moderate the activity of their genes. Ladeira *et al.*[92] demonstrated a highly efficient siRNA delivery system into human and murine cells using MWNTs. The MWNT–siRNA delivery system demonstrated nonspecific toxicity and transfection efficiency greater than 95%. The potential for siRNA delivery was demonstrated into different types of cells, including hard-to-transfect cells, such as neuronal cells and cardiomyocytes.

Fig. 9a shows the G band MWNT imaging in the studied sample, demonstrating the presence of MWNTs inside neo-natal cardiomyocytes, confirming the ability of MWNTs to enter this cell. The spectrum in Fig. 9b was taken at the location indicated by the arrow in Fig. 9a. The large D band is consistent with the MWNT material they used, *i.e.* short and carboxylated-MWNT–siRNA, which represents a very effective RNA interference carrier to different cell types, providing an efficient silencing of the target gene with high specificity and large reduction in toxicity.[92]

### 3.2 Amorphous carbons in soil science

Although tropical soils are generally unfertile due to high temperatures and heavy rains, the pre-Columbian indigenous groups living in the Amazonian forest subsisted on agriculture in addition to hunting, fishing and gathering activities.[93] Their way of life generated areas of highly fertile soils rich in plant nutrients known as "Terra Preta de Índio" (Amazonian Dark Earth).[94] These soils are dated up to 7000 years old, and it is generally accepted that they are anthropogenic in origin, although it is not clear whether this was intentional or was a byproduct of Indian activities.[95] "Terra Preta de Índio" (TPI) is more common in

sites at the Amazon basin,[96–99] but it can also be found throughout the humid tropics, *e.g.* in other regions of South America and Africa.[100,101] Therefore, these anthropogenic Amazonian soils provide a potential model for a sustainable land-use system in the humid tropics. The key issue behind its recalcitrance is the large amount of stable sp$^2$ carbon-based materials, responsible for its high fertility over long periods of usage. Soil scientists are trying to create "Terra Preta Nova" (TPN – New Dark Earth) by adding charcoal as a soil conditioner.

In sp$^2$ layered carbons, Raman spectroscopy can be used to measure the nanocrystallite dimensions, which are defined by the in-plane crystallite size ($L_a$).[8,63,64,102,103] Considering that Raman spectroscopy comes predominantly from the resonant sp$^2$ carbon, insight into the in-plane dimension $L_a$ of the nanocrystalline structures composing these TPI-carbon grains can be obtained from the analysis of their G peak full-width at half maximum ($\Gamma_G$), given by

$$L_a \text{ (nm)} = 560/[\Gamma_G - 11], \qquad (9)$$

which is valid for nanocrystalline graphite.[64]

The importance of the $\Gamma_G$ Raman analysis in the TPI science is demonstrated in Fig. 10, where the results from
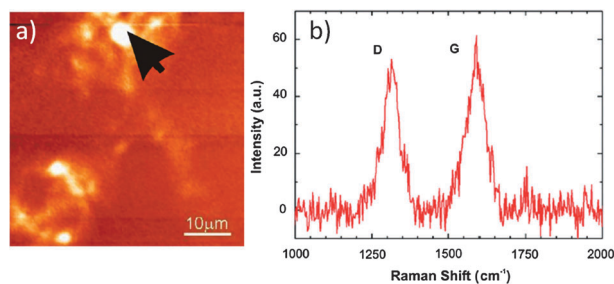
**Fig. 9** CNTs can be uptaken by neonatal cardiomyocytes. (a) Representative Raman spectrum of neonatal cardiomyocytes exposed to MWNTs (0.025 mg ml$^{-1}$) for 48 h. The G band peak at 1580 cm$^{-1}$ was used for MWNT imaging inside this cell. (b) Raman spectra taken at the location indicated by the arrow in panel (a). The presence of the D and G bands is indicated here.[92]
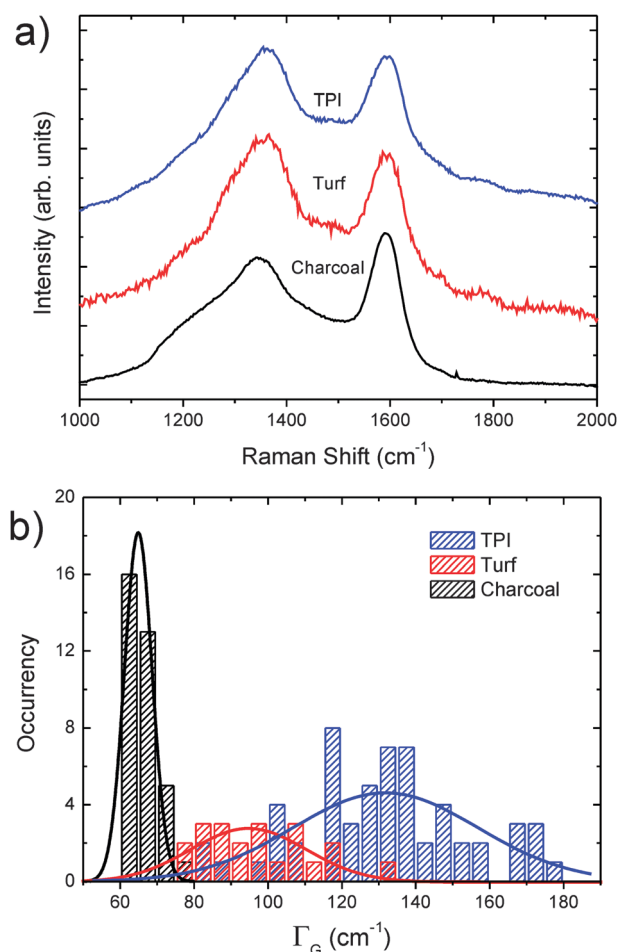
**Fig. 10** (a) Raman spectra from TPI-carbon (top), carbon from turf (middle) and charcoal (bottom). (b) Statistical analysis of the $\Gamma_G$ from TPI-carbons, carbon from turf and charcoal. Data obtained using a 632.8 nm laser.[104]

the TPI-carbons are compared with results from (i) turf (or peat), which is another highly productive black soil formed by the accumulation of partially decayed vegetative matter and (ii) different samples of charcoal from different vegetable sources that are intentionally produced for TPN ("Terra Preta Nova") generation [see spectra in Fig. 10a].[104,105] Fig. 10b plots the measured distribution for $\Gamma_G$. The charcoal produced for TPN generation did not exhibit the expected carbon nanostructure because $\Gamma_G$ was too small (*i.e.* $L_a$ was too large). Considering eqn (9), the crystallite size distribution for a piece of charcoal was typically found between 8 and 12 nm, while the TPI-carbons were found in the 3–8 nm range.[104,105] This provides inputs from nanotechnology, based on Raman spectroscopy, for work that is needed in the laboratory to generate a nano-carbon structure that could be suitable for the TPN generation.

## 4. Conclusion and challenges

In this article we quickly pointed out the impressive development in the Raman spectroscopy of graphene-like nanocarbons in the last decade (2000–2009), and discussed in more detail the state-of-the-art results in the new decade, starting in 2010. The experiments are becoming more and more sophisticated due to the fast development of nanotechnology. Applications are already in place in cross-related fields, such as biotechnology and soil science. Basically, wherever carbon nano-structures are used, Raman spectroscopy can help with detecting critical issues in characterizing samples. Spectral imaging can be used to detect and locate carbon nanostructures inside biological materials for example, while Raman frequency shifts indicate and quantify carbon–environment interactions.

Mature materials, like carbon nanotubes, require the development of innovative state-of-the-art samples and complex instrumentation for developing impactful scientific work. Furthermore, the proximity of applications asks for more systematic metrology-oriented works. The avenue for new science leaves on using the carbon nanotube as a prototype for developing nanometrology and for studying environmental effects on the nanoscale.

Graphene has now reached a state of maturity as well. It has provided a perfect surface for studies which were not possible before, opening a new avenue for the development of surface science. Graphene opens also an important route for the development of near-field scattering in two-dimensional systems, which is in its infancy. However, in the case of near-field Raman spectroscopy, the high resolution ($\sim$10 nm) instrumental setups are still at the home-built development stage. The main challenge for TERS is the development of new and robust instrumentation for achieving ready to use systems. For the moment the home-built systems require extensive work on the instrument for very limited results on materials science.

Finally, the study of new materials is always a challenge that promises important new findings. Furthermore, when the material is a novelty, simpler experiments are usually very informative and might represent breakthroughs. One route is on new carbon nanostructures, like nanocones, which hold strong promises of several interesting mechanical, thermal and electronic properties, but have been addressed mostly theoretically.[106–109]

Another route is using the knowledge on graphene to study other few layer materials, like $MoS_2$ and BN.[110–112] Raman spectroscopy is likely to play an important role here as well as in more complex transition metal dichalcogenides.

## Acknowledgements

## Notes and references

1 V. Raman, *The Molecular Scattering of Light*, Nobel Lecture, 1930.
2 A. Jorio, M. S. Dresselhaus, R. Saito and G. Dresselhaus, *Raman Spectroscopy in Graphene Related Systems*, WILEY-VCH, Weinheim, 2011, and references contained therein.
3 F. Tuinstra and J. L. Koenig, *J. Chem. Phys.*, 1970, **53**, 1126.
4 M. S. Dresselhaus and R. Kalish, *Ion Implantation in Diamond Graphite and Related Materials*, Springer-Verlag, Springer Series in Materials Science, Berlin, 1992.
5 M. S. Dresselhaus, G. Dresselhaus and P. C. Eklund, *Science of Fullerenes and Carbon Nanotubes*, Academic, New York, NY, 1996.
6 A. Jorio, R. Saito, G. Dresselhaus and M. S. Dresselhaus, *Phil. Trans. R. Soc. A*, 2004, **362**(1824), 2311–2336.
7 R. Saito, M. Hofmann, G. Dresselhaus, A. Jorio and M. S. Dresselhaus, *Adv. Phys.*, 2011, **60**(3), 413–550, and references contained therein.
8 A. C. Ferrari and J. Robertson, *Phys. Rev. B: Condens. Matter Mater. Phys.*, 2000, **61**, 14095.
9 C. Thomsen and S. Reich, *Phys. Rev. Lett.*, 2000, **85**, 5214.
10 R. Saito, A. Jorio, A. G. Souza Filho, G. Dresselhaus, M. S. Dresselhaus and M. A. Pimenta, *Phys. Rev. Lett.*, 2002, **88**, 027401.
11 A. M. Rao, A. Jorio, M. A. Pimenta, M. S. S. Dantas, R. Saito, G. Dresselhaus and M. S. Dresselhaus, *Phys. Rev. Lett.*, 2000, **84**, 1820–1823.
12 E. B. Barros, A. Jorio, G. G. Samsonidze, R. B. Capaz, A. G. Filho, J. M. Filho, G. Dresselhaus and M. S. Dresselhaus, *Phys. Rep.*, 2006, **431**, 261–302.
13 A. Jorio, R. Saito, J. H. Hafner, C. M. Lieber, M. Hunter, T. McClure, G. Dresselhaus and M. S. Dresselhaus, *Phys. Rev. Lett.*, 2001, **86**, 1118–1121.
14 L. G. Cançado, M. A. Pimenta, R. A. Neves, G. Medeiros-Ribeiro, T. Enoki, Y. Kobayashi, K. Takai, K. Fukui, M. S. Dresselhaus, R. Saito and A. Jorio, *Phys. Rev. Lett.*, 2004, **93**, 047403.
15 A. G. Souza Filho, *et al.*, *Phys. Rev. B: Condens. Matter Mater. Phys.*, 2002, **65**, 085417.
16 A. C. Ferrari, J. C. Meyer, V. Scardaci, C. Casiraghi, M. Lazzeri, M. Mauri, S. Piscanec, D. Jiang, K. S. Novoselov, S. Roth and A. K. Geim, *Phys. Rev. Lett.*, 2006, **97**, 187401.
17 A. Hartschuh, E. J. Sánchez, X. S. Xie and L. Novotny, *Phys. Rev. Lett.*, 2003, **90**, 95503.
18 L. G. Cançado, M. A. Pimenta, B. R. A. Neves, M. S. S. Dantas and A. Jorio, *Phys. Rev. Lett.*, 2004, **93**, 247401.
19 C. Casiraghi, A. Hartschuh, H. Qian, S. Piscanec, C. Georgi, A. Fasoli, K. S. Novoselov, D. M. Basko and A. C. Ferrari, *Nano Lett.*, 2009, **9**, 1433–1441.
20 C. Fantini, A. Jorio, M. Souza, M. S. Strano, M. S. Dresselhaus and M. A. Pimenta, *Phys. Rev. Lett.*, 2004, **93**, 147406.
21 H. Telg, J. Maultzsch, S. Reich, F. Hennrich and C. Thomsen, *Phys. Rev. Lett.*, 2004, **93**, 177401.
22 P. T. Araujo, S. K. Doorn, S. Kilina, S. Tretiak, E. Einarsson, S. Maruyama, H. Chacham, M. A. Pimenta and A. Jorio, *Phys. Rev. Lett.*, 2007, **98**, 067401.
23 S. K. Doorn, P. T. Araujo, K. Hata and A. Jorio, *Phys. Rev. B: Condens. Matter Mater. Phys.*, 2008, **78**, 165408.
24 R. Pfeiffer, F. Simon, H. Kuzmany and V. N. Popov, *Phys. Rev. B: Condens. Matter Mater. Phys.*, 2005, **72**, 161404.

25 A. G. Souza Filho, A. Jorio, Ge. G. Samsonidze, G. Dresselhaus, R. Saito and M. S. Dresselhaus, *Nanotechnology*, 2003, **14**(10), 1130–1139.

26 P. Corio, A. Jorio, N. Demir and M. S. Dresselhaus, *Chem. Phys. Lett.*, 2004, **392**, 396–402.

27 S. Piscanec, M. Lazzeri, M. Mauri, A. C. Ferrari and J. Robertson, *Phys. Rev. Lett.*, 2004, **93**, 185503.

28 D. A. Das, S. Pisana, B. Chakraborty, S. Piscanec, S. K. Saha, U. V. Waghmare, K. S. Novoselov, H. R. Krishnamurthy, A. K. Geim, A. C. Ferrari and A. K. Sood, *Nat. Nanotechnol.*, 2008, **3**, 210.

29 M. Kalbac, H. Farhat, L. Kavan, J. Kong and M. S. Dresselhaus, *Nano Lett.*, 2008, **8**, 2532–2537.

30 J. S. Park, K. Sasaki, R. Saito, W. Izumida, M. Kalbac, H. Farhat, G. Dresselhaus and M. S. Dresselhaus, *Phys. Rev. B: Condens. Matter Mater. Phys.*, 2009, **80**, 081402.

31 J. Jiang, R. Saito, K. Sato, J. Park, Ge. Samsonidze, A. Jorio, G. Dresselhaus and M. S. Dresselhaus, *Phys. Rev. B: Condens. Matter Mater. Phys.*, 2007, **75**, 035405.

32 I. O. Maciel, N. Anderson, M. A. Pimenta, A. Hartschuh, H. H. Qian, M. Terrones, H. Terrones, J. Campos-Delgado, A. M. Rao, L. Novotny and A. Jorio, *Nat. Mater.*, 2008, **7**, 878.

33 P. T. Araujo, I. O. Maciel, P. B. C. Pesce, M. A. Pimenta, S. K. Doorn, H. Qian, A. Hartschuh, M. Steiner, L. Grigorian, K. Hata and A. Jorio, *Phys. Rev. B: Condens. Matter Mater. Phys.*, 2008, **77**, 241403.

34 P. T. Araujo, A. Jorio, M. S. Dresselhaus, K. Sato and R. Saito, *Phys. Rev. Lett.*, 2009, **103**, 146802.

35 E. J. Mele, *Phys. Rev. B: Condens. Matter Mater. Phys.*, 2010, **81**, 161405.

36 G. Li, A. Luican, J. M. B. Lopes dos Santos, A. H. Castro Neto, A. Reina, J. Kong and E. Y. Andrei, *Nat. Phys.*, 2010, **6**, 109–113.

37 W. Kohn and J. M. Luttinger, *Phys. Rev. Lett.*, 1965, **15**, 524–526.

38 T. M. Rice and G. K. Scott, *Phys. Rev. Lett.*, 1975, **35**, 120–123.

39 M. Fleck, A. M. Oleś and L. Hedin, *Phys. Rev. B: Condens. Matter Mater. Phys.*, 1997, **56**, 3159–3166.

40 V. Carozo, C. M. Almeida, E. H. M. Ferreira, L. G. Cançado, C. A. Achete and A. Jorio, *Nano Lett.*, 2011, **11**, 4527–4534.

41 A. K. Gupta, Y. Tang, V. H. Crespi and P. C. Eklund, *Phys. Rev. B: Condens. Matter Mater. Phys.*, 2010, **82**, 241406.

42 A. Righi, S. D. Costa, H. Chacham, C. Fantini, P. Venezuela, C. Magnuson, L. Colombo, W. S. Bacsa, R. S. Ruoff and M. A. Pimenta, *Phys. Rev. B: Condens. Matter Mater. Phys.*, 2011, **84**, 241409.

43 R. Podila, R. Rao, R. Tsuchikawa, M. Ishigami and A. M. Rao, *ACS Nano*, 2012, **6**(7), 5784–5790.

44 Z. Ni, L. Liu, Y. Wang, Z. Zheng, L.-J. Li, T. Yu and Z. Shen, *Phys. Rev. B: Condens. Matter Mater. Phys.*, 2009, **80**, 125404.

45 R. W. Havener, H. Zhuang, L. Brown, R. G. Hennig and J. Park, *Nano Lett.*, 2012, **12**, 3162–3167.

46 K. Kim, S. Coh, L. Z. Tan, W. Regan, J. M. Yuk, E. Chatterjee, M. F. Crommie, M. L. Cohen, S. G. Louie and A. Zettl, *Phys. Rev. Lett.*, 2012, **108**, 246103–246108.

47 S. Reich, C. Thomsen and P. Ordejón, *Phys. Rev. B: Condens. Matter Mater. Phys.*, 2002, **65**, 153407.

48 S. B. Cronin, A. K. Swan, M. S. Ünlü, B. B. Goldberg, M. S. Dresselhaus and M. Tinkham, *Phys. Rev. Lett.*, 2004, **93**, 167401–167405.

49 B. Gao, J. Lai, L. Xi, L. Zhang and Z. Liu, *J. Phys. Chem. C*, 2008, **112**(51), 20123–20125.

50 A. G. Souza Filho, N. Kobayashi, J. Jiang, A. Grüneis, R. Saito, S. B. Cronin, J. Mendes Filho, Ge. G. Samsonidze, G. Dresselhaus and M. S. Dresselhaus, *Phys. Rev. Lett*, 2005, **95**, 217403–217407.

51 X. Yang, G. Wu and J. Dong, *Appl. Phys. Lett.*, 2006, **89**, 113101–113103.

52 M. Yao, Z. Wang, B. Liu, Y. Zou, S. Yu, W. Lin, Y. Hou, S. Pan, M. Jin, B. Zou, T. Cui, G. Zou and B. Sundqvist, *Phys. Rev. B: Condens. Matter Mater. Phys.*, 2008, **78**(20), 205411.

53 A. L. Aguiar, E. B. Barros, R. B. Capaz, A. G. Souza Filho, P. T. C. Freire, J. Mendes Filho, D. Machon, Ch. Caillier, Y. A. Kim, H. Muramatsu, M. Endo and A. San-Miguel, *J. Phys. Chem. C*, 2011, **115**, 5378–5384.

54 P. T. Araujo, N. M. Barbosa Neto, H. Chacham, S. S. Carara, J. S. Soares, A. D. Souza, L. G. Cançado, A. B. de Oliveira, R. J. C. Batista, E. Joselevich, M. S. Dresselhaus and A. Jorio, *Nano Lett.*, 2012, **12**(8), 4110–4116.

55 B. T. Kelly, *Physics of Graphite*, Applied Science Publishers, London and New Jersey, 1981.

56 M. A. Pimenta, G. Dresselhaus, M. S. Dresselhaus, L. G. Cançado, A. Jorio and R. Saito, *Phys. Chem. Chem. Phys.*, 2007, **9**(11), 1276–1290.

57 M. M. Lucchese, F. Stavale, E. H. Martins Ferreira, C. Vilani, M. V. O. Moutinho, R. B. Capaz, C. A. Achete and A. Jorio, *Carbon*, 2010, **48**(5), 1592–1597.

58 E. H. Martins Ferreira, M. V. O. Moutinho, F. Stavale, M. M. Lucchese, R. B. Capaz, C. A. Achete and A. Jorio, *Phys. Rev. B: Condens. Matter Mater. Phys.*, 2010, **82**, 125429.

59 A. Jorio, M. M. Lucchese, F. Stavale, E. H. M. Ferreira, M. V. O. Moutinho, R. B. Capaz and C. A. Achete, *J. Phys.: Condens. Matter*, 2010, **22**, 334204.

60 A. Jorio, M. M. Lucchese, F. Stavale and C. A. Achete, *Phys. Stat. Solidi (b)*, 2009, **246**(11, 12), 2689–2692.

61 D. Teweldebrhan and A. A. Balandin, *Appl. Phys. Lett.*, 2009, **94**, 13101.

62 G. Compagnini, F. Giannazzo, S. Sonde, V. Raineri and E. Rimini, *Carbon*, 2009, **47**(14), 3201–3207.

63 L. G. Cançado, K. Takai, T. Enoki, M. Endo, Y. A. Kim, H. Mizusaki, A. Jorio, L. N. Coelho, R. Magalhaes-Paniago and M. A. Pimenta, *Appl. Phys. Lett.*, 2006, **88**, 163106.

64 L. G. Cançado, A. Jorio and M. A. Pimenta, *Phys. Rev. B: Condens. Matter Mater. Phys.*, 2007, **76**, 064304–064310.

65 L. G. Cançado, R. Beams, L. Novotny, Optical measurement of the phase-breaking length in graphene, arXiv: 0802.3709.

66 A. K. Gupta, T. J. Russin, H. R. Gutierrez and P. C. Eklund, *ACS Nano*, 2009, **3**(1), 45–52.

67 L. G. Cançado, A. Jorio, E. H. Martins Ferreira, F. Stavale, C. A. Achete, R. Capaz, M. Moutinho, A. Lombardo, T. Kulmala and A. C. Ferrari, *Nano Lett.*, 2011, **11**(8), 3190–3196.

68 B. S. Archanjo, A. P. M. Barboza, B. R. A. Neves, L. M. Malard, E. H. M. Ferreira, J. C. Brant, E. S. Alves, F. Plentz, V. Carozo, B. Fragneaud, I. O. Maciel, C. M. Almeida, A. Jorio and C. A. Achete, *Nanotechnology*, 2012, **23**, 255305.

69 B. S. Archanjo, I. O. Maciel, E. H. M. Ferreira, S. B. Peripolli, J. C. Damasceno, C. A. Achete and A. Jorio, *Ultramicroscopy*, 2011, **111**, 1338.

70 P. B. C. Pesce, P. T. Araujo, P. Nikolaev, S. K. Doorn, K. Hata, R. Saito, M. S. Dresselhaus and A. Jorio, *Appl. Phys. Lett.*, 2010, **96**, 051910.

71 P. T. Araujo, P. B. C. Pesce, M. S. Dresselhaus, K. Sato, R. Saito and A. Jorio, *Phys. E*, 2010, **42**, 1251.

72 M. Born and E. Wolf, *Principles of Optics*, Cambridge University Press, Cambridge, 1999.

73 L. Novotny and B. Hecht, *Principles of Nano-Optics*, Cambridge University Press, Cambridge, 2006.

74 L. G. Cançado, A. Hartschuh and L. Novotny, *J. Raman Spectrosc.*, 2009, **40**, 1420–1426.

75 N. Hayazawa, T. Yano, H. Watanabe, Y. Inouye and S. Kawata, *Chem. Phys. Lett.*, 2003, **376**, 174–180.

76 N. Anderson, A. Hartschuh, S. Cronin and L. Novotny, *J. Am. Chem. Soc.*, 2005, **127**, 2533–2537.

77 A. Hartschuh, H. Qian, A. J. Meixner, N. Anderson and L. Novotny, *Nano Lett.*, 2005, **5**, 2310–2313.

78 Y. Saito, N. Hayazawa, H. Kataura, T. Murakami, K. Tsukagoshi, Y. Inouye and S. Kawata, *Chem. Phys. Lett.*, 2005, **410**, 136–141.

79 N. Anderson, A. Hartschuh and L. Novotny, *Nano Lett.*, 2007, **7**, 577–582.

80 H. Qian, P. T. Araujo, C. Georgi, T. Gokus, N. Hartmann, A. A. Green, A. Jorio, M. C. Hersam, L. Novotny and A. Hartschuh, *Nano Lett.*, 2008, **8**, 2706–2711.

81 G. G. Hoffmann, G. de With and J. Loos, *Macromol. Symp.*, 2008, **265**, 1–11.

82 Y. Saito, P. Verma, K. Masui, Y. Inouye and S. Kawata, *J. Raman Spectrosc.*, 2009, **40**, 1434–1440.

83 K. F. Domke and B. Pettinger, *J. Raman Spectrosc.*, 2009, **40**, 1427–1433.

84 V. Snitka, R. D. Rodrigues and V. Lendraitis, *Microelectron. Eng.*, 2011, **88**, 2759–2762.

85 J. Stadler, T. Schmid and R. Zenobi, *ACS Nano*, 2011, **5**, 8442–8448.

86  L. G. Cançado, A. Jorio, A. Ismach, E. Joselevich, A. Hartschuh and L. Novotny, *Phys. Rev. Lett.*, 2009, **103**, 186101.

87  R. V. Maximiano, R. Beams, L. Novotny, A. Jorio and L. G. Cançado, *Phys. Rev. B: Condens. Matter Mater. Phys.*, 2012, **85**, 235434.

88  N. W. Kam, Z. Liu and H. Dai, *J. Am. Chem. Soc.*, 2005, **127**, 12492.

89  K. Rege, G. Viswanathan, G. Zhu, A. Vijayaraghavan, P. M. Ajayan and J. S. Dordick, *Small*, 2006, **2**, 718–22.

90  Z. Zhang, X. Yang, Y. Zhang, B. Zeng, S. Wang, T. Zhu, R. B. Roden, Y. Chen and R. Yang, *Clin. Cancer Res.*, 2006, **12**, 4933–4939.

91  R. Krajcik, A. Jung, A. Hirsch, W. Neuhuber and O. Zolk, *Biochem. Biophys. Res. Commun.*, 2008, **369**, 595–602.

92  M. S. Ladeira, V. A. Andrade, E. R. Morais, C. J. Aguiar, E. R. Moraes, J. S. Soares, E. E. Silva, R. G. Lacerda, L. O. Ladeira, A. Jorio, P. Lima, M. F. Leite, R. R. Resende and S. Guatimosim, *Nanotechnology*, 2010, **21**, 385101.

93  M. F. Simões, A Pré-História da Bacia Amazônica: Uma tentativa de reconstituição, in *Cultura Indígena, Textos e Catálogo, Semana do Índio*, Museu Goeldi, Belém, 1982, pp. 5–21.

94  D. C. Kern, Geoquímica e Pedogeoquímica em sítios Arqueológicos com terra preta na Floresta Nacional de Caxiuanã, PhD Thesis, Universidade Federal do Pará, Belém Portel-PA, Brazil, 1996.

95  N. J. H. Smith, *Ann. Assoc. Am. Geogr.*, 1980, **70**(4), 553–566.

96  N. P. S. Falcão, N. Comerford and J. Lehmann, Determining nutrient bioavailability of amazonian dark earth soils – methodological challenges, in *Amazonian Dark Earths; Origins, Properties, Management*, ed. J. Lehmann, D. C. Kern, B. Glaser and W. I. Woods, Kluwer Academic Publishers, 2003, pp. 255–270.

97  B. Glaser, J. Lehmann and W. Zech, *Biol. Fertil. Soils*, 2002, **35**, 219–230.

98  B. Glaser, *Philos. Trans. R. Soc., A*, 2007, **362**, 187–196.

99  E. Marris, *Nature*, 2006, **442**, 626–628.

100  A. C. Blackmore, M. T. Mentis and R. J. Scholes, *J. Biogeogr.*, 1990, **17**, 463–470.

101  W. Zech, L. Haumaier and R. Hempfling, Ecological aspects of soil organic matter in tropical land use, in *Humic Substances in Soil and Crop Sciences: Selected Readings*, ed. P. McCarthy, C. E. Clapp, R. L. Malcolm and P. R. Bloom, American Society of Agronomy and Soil Science Society of America, Madison, WI, USA, 1990, pp. 187–202.

102  A. C. Ferrari and J. Robertson, *Phys. Rev. B: Condens. Matter Phys.*, 2001, **64**, 075414.

103  K. Takai, M. Oga, H. Sato, T. Enoki, Y. Ohki, A. Taomoto, K. Suenaga and S. Iijima, *Phys. Rev. B: Condens. Matter Mater. Phys.*, 2003, **67**, 214202.

104  A. Jorio, J. Ribeiro-Soares, L. G. Cançado, N. P. S. Falcao, H. F. Dos Santos, D. L. Baptista, E. H. Martins Ferreira, B. S. Archanjo and C. A. Achete, *Soil Tillage Res.*, 2012, **122**, 61–66.

105  J. Ribeiro-Soares, L. G. Cançado, N. P. S. Falcão, E. H. Martins Ferreira, C. A. Achete and A. Jorio, *J. Raman Spec.*, 2012, DOI: 10.1002/jrs.4191.

106  J.-C. Charlier and G.-M. Rignanese, *Phys. Rev. Lett.*, 2001, **86**, 5970–5973.

107  S. P. Jordan and V. H. Crespi, *Phys. Rev. Lett.*, 2004, **93**, 255504.

108  N. Yang, G. Zhang and B. Li, *Appl. Phys. Lett.*, 2008, **93**, 243111–243111.

109  M. Yudasaka, S. Iijima and V. H. Crespi, *Top. Appl. Phys.*, 2008, **111**, 605–629.

110  J. N. Coleman, M. Lotya, A. O' Neill, S. D. Bergin, P. J. King, U. Khan, K. Young, A. Gaucher, S. De, R. J. Smith, I. V. Shvets, S. K. Arora, G. Stanton, H.-Y. Kim, K. Lee, G. T. Kim, G. S. Duesberg, T. Hallam, J. J. Boland, J. J. Wang, J. F. Donegan, J. C. Grunlan, G. Moriarty, A. Shmeliov, R. J. Nicholls, J. M. Perkins, E. M. Grieveson, K. Theuwissen, D. W. McComb, P. D. Nellist and V. Nicolosi, *Science*, 2011, **331**, 568.

111  B. Radisavljevic, A. Radenovic, J. Brivio, V. Giacometti and A. Kis, *Nat. Nanotechnol.*, 2011, **6**, 147.

112  R. V. Gorbachev, I. Riaz, R. R. Nair, R. Jalil, L. Britnell, B. D. Belle, E. W. Hill, K. S. Novoselov, K. Watanabe, T. Taniguchi, A. K. Geim and P. Blake, *Small*, 2011, **7**, 465.